Understanding seismic heterogeneities in the lower mantle beneath the Americas from seismic tomography and plate tectonic history

Yong Ren,[1] Eléonore Stutzmann,[1] Robert D. van der Hilst,[2] and Jean Besse[3]

[1] We combine results from seismic tomography and plate motion history to investigate slabs of subducted lithosphere in the lower mantle beneath the Americas. Using broadband waveform cross correlation, we measured 37,000 differential P and S traveltimes, 2000 PcP-P and ScS-S times along a wide corridor from Alaska to South America. We invert the data simultaneously to obtain P and S wave velocity models. We interpret slab structures and unravel subduction history by comparing our V_S tomographic images with reconstructed plate motion from present-day up to 120 Myr. Convergence of the Pacific with respect to the Americas is computed using either (1) the Pacific and Indo-Atlantic hot spot reference frames or (2) the plate circuit passing through Antarctica. Around 800 km depth, four distinctive fast anomalies can be associated with subduction of the Nazca, Cocos, and Juan de Fuca plates beneath South, Central, and North America, respectively, and of the Pacific plate beneath the Aleutian island arc. The large fast anomalies in the lowermost mantle, which are most pronounced in the S wave models, can be associated with Late Cretaceous subduction of the Farallon plate beneath the Americas. Near 2000 km depth, the images record the post-80 Myr fragmentation of the proto-Farallon plate into the Kula plate in the north and the Farallon plate in the northeast. Near 1000 km depth, we infer separate fast anomalies interpreted as the Kula-Pacific, Juan de Fuca, and Farallon slabs. This interpretation is consistent with the volume and length of slabs estimated from the tomographic images and the plate history reconstruction.

1. Introduction

[2] Tomographic images provide us with snapshots of solid-state flow in Earth's mantle and can help determine if and how slabs of subducted lithospheric plates sink into Earth's lower mantle. In the transition zone and in the lowermost mantle the large-scale variation in shear wave speed is dominated by a spherical harmonic degree 2 pattern, and the fast anomalies are mainly located around the Pacific [*Masters et al.*, 1982; *Hager et al.*, 1985; *Dziewonski and Woodhouse*, 1987] where recent subduction has occurred and remnant slabs are expected to be found [*Richards and Engebretson*, 1992; *Ricard et al.*, 1993; *Steinberger*, 2000].

[3] During the last decade, improvements in imaging methodology and data quality and quantity have produced increasingly detailed images of slabs of subducted litho-spheric plates [e.g., *van der Hilst et al.*, 1997; *Grand et al.*, 1997; *Vasco and Johnson*, 1998; *Bijwaard et al.*, 1998; *Kennett et al.*, 1998; *Kárason and van der Hilst*, 2001; *Grand*, 2002; *Zhao*, 2004], and several authors have noted the good correlation between narrow regions of fast seismic anomalies in the lower mantle and subduction locations during Cenozoic and Mesozoic eras [e.g., *Grand*, 1994; *Grand et al.*, 1997; *Lithgow-Bertelloni and Richards*, 1998; *Bunge and Grand*, 2000].

[4] Tomographic images have shown that many, but not all, slabs descend into the lower mantle [e.g., *van der Hilst*, 1990; *van der Hilst et al.*, 1997]. Depending on several parameters, including the rate of subduction and oceanward trench migration [e.g., *Christensen and Yuen*, 1984; *Gurnis and Hager*, 1988; *Kincaid and Olson*, 1987; *van der Hilst and Seno*, 1993; *Griffiths et al.*, 1995; *Davies*, 1995], the negative Clapeyron slope of the isochemical (postspinel) phase transition and the increase of viscosity near 660 km depth can distort the trajectory of mantle flow across the transition from upper to lower mantle and even delay the further descent of slabs. Slabs may not all sink to the very base of the mantle [*van der Hilst and Kárason*, 1999; *Albarède and van der Hilst*, 2002]. Some may be deflected around 670 km depth (see *Fukao et al.* [2001] for a review),

[1]Laboratoire de Sismologie, Institut de Physique du Globe de Paris, Paris, France.
[2]Department of Earth, Atmospheric, and Planetary Sciences, Massachusetts Institute of Technology, Cambridge, Massachusetts, USA.
[3]Laboratoire de Paléomagnétisme, Institut de Physique du Globe de Paris, Paris, France.
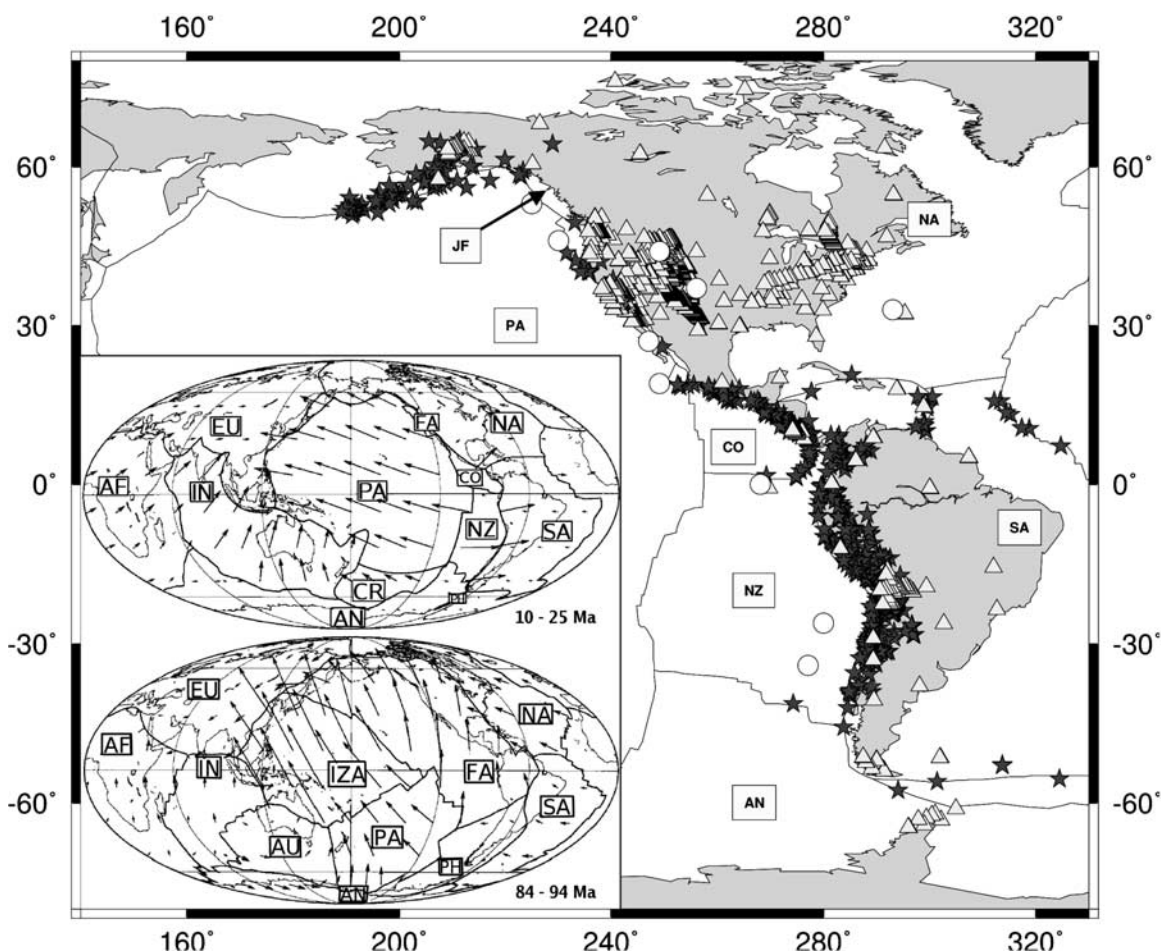
Figure 1. Location map of earthquakes (black stars) and seismic stations (white triangles) used in this study. Hot spots are depicted with white circles. The inserts represent plate boundary maps at 10–25 Myr and 84–94 Myr from *Lithgow-Bertelloni and Richards* [1998].

but those that do sink into the lower mantle can reach the bottom of it some 80–100 Myr after subduction [e.g., *Steinberger*, 2000]. The actual evolution of tectonic plates over time (including variable rates and directions of subduction and the merging or breaking up of tectonic plates) and the dynamic effects of radial changes in mantle viscosity and (mineralogical) phase can combine to produce mantle flow trajectories that are far more complex than expected from simple convection modeling [see, e.g., *Tan et al.*, 2002]. Combined interpretation of tomographic images and reconstruction of the history of plate motion can thus help meet the challenge of understanding the ultimate fate of slabs.

[5] We investigate the mantle beneath North, Central, and South America: this region has been shaped by interaction between different oceanic plates and between oceanic and continental plates. Oceanic plates have subducted beneath the Americas for almost 400 Myr [*Storey*, 1995]. A detailed history of the plate motions is given by *Richards and Engebretson* [1992] and *Lithgow-Bertelloni and Richards* [1998] and is summarized in Figure 1. In the Mesozoic era, the ancient Izanagi, Farallon, Phoenix, and Pacific plates made up most of the Pacific Ocean; the Pacific plate and fragments of Farallon plate still exist today whereas other plates have entirely

disappeared. The Cenozoic era is marked by the interaction between three major oceanic plates: the Farallon, Kula, and Pacific plates. The Farallon plate has been successively broken up to form a number of smaller plates upon subduction under the Americas. Farallon plate fragmentation during the Cretaceous produced the Kula plate in the north which disappeared from Earth's surface near 48 Myr; later, the remaining part of the Farallon plate fragmented into the Nazca, Cocos, and Juan de Fuca plates, which define the present-day subduction zones in the region (Figure 1).

[6] With certain assumptions, seismically fast anomalies at a given depth in the mantle can be correlated with slab fragments due to past episodes of subduction. *Grand* [1994] showed that beneath South America no fast (slab like) anomalies are present beneath 1300 km depth, which he explained by the reduction in convergence of the Nazca/Farallon plate prior to 60 Myr. *Bunge and Grand* [2000] showed that the slab bend observed in tomographic images between 900 and 1500 km depth beneath the eastern part of North America can be explained by low-angle subduction of young lithosphere created between the separating Kula and Farallon plates during the Mesozoic. This low-angle subduction had been invoked
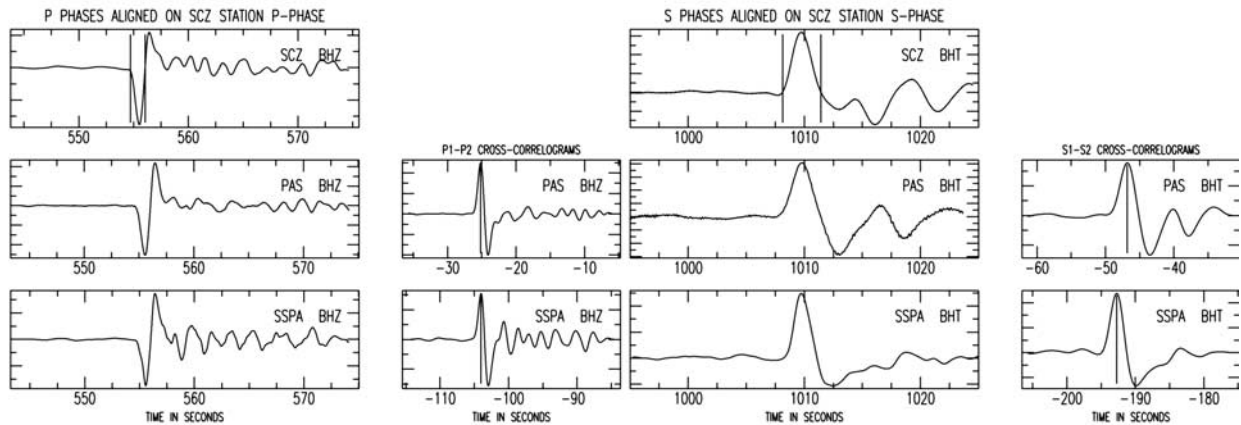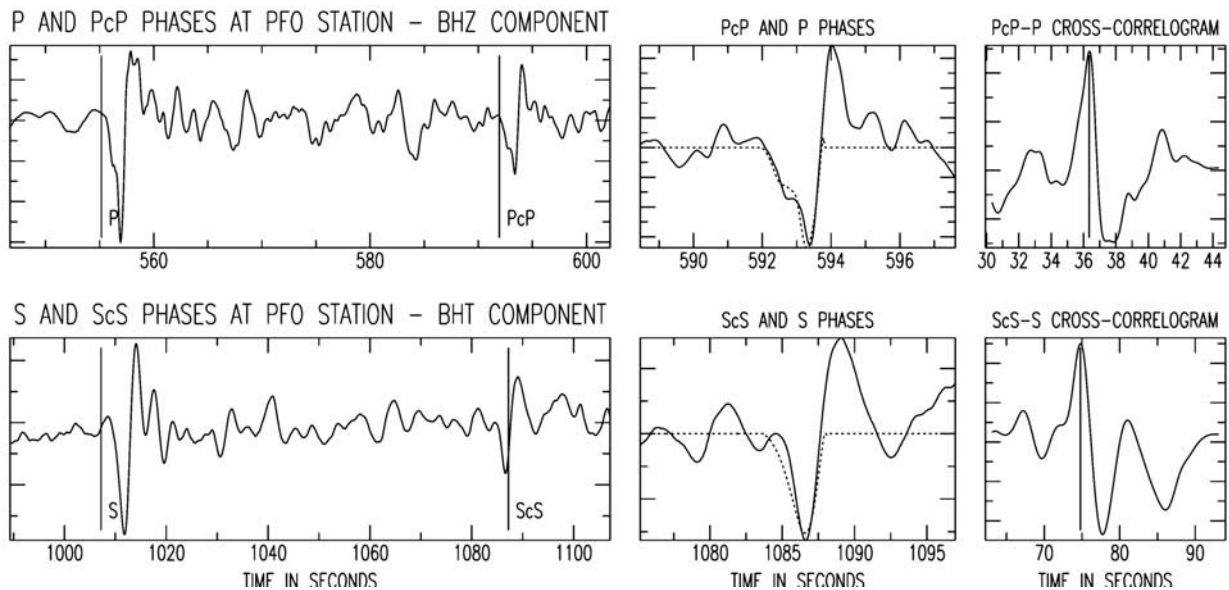
(a) Differential travel times P1-P2 and S1-S2

(b) Differential travel times PcP-P and ScS-S

Figure 2. (a) Example of data for an event on 28 August 1999 (latitude $-1.26°$N, longitude $-77.47°$E and depth 198 km). (left) P_1-P_2 differential traveltime measurement. (top) Windowed P arrival for the reference station and (bottom) P arrivals recorded by two other stations and the cross correlograms. (right) Same for S_1-S_2 measurement. (b) Example of data for an event on 4 November 1994 (latitude $-9.44°$N, longitude $-71.27°$E and depth 591 km). (top) PcP-P differential traveltime measurement; (left) vertical seismogram with the phases P and PcP, (middle) windowed PcP waveform and superposition of P and PcP waveforms, (right) cross correlograms (bottom) Same for ScS-S measurement.

independently to explain the Rocky Mountain uplift during the Laramid orogeny [e.g., *Bird*, 1979, 1984].

[7] The aim of this paper is to define the slab characteristics associated with the different subducted plates. The geometry of the subducted plates is inferred through tomographic inversion of a large number of P and S wave traveltimes, measured from broad band seismograms using waveform cross correlation. We use plate reconstructions to help identify the slab fragments in the tomographic model thus obtained. The great circle corridor from the Aleutian arc to South America has a fairly continuous distribution of earthquakes and stations, which enables us to derive P and S wave speed models from a joint inversion with similar path

coverage for P and S type data [*Saltzer et al.*, 2004]. The relative variations in V_P and V_S provide constraints on the thermal or compositional nature of the seismic anomalies associated with the subducted slabs and the ambient mantle, but those results will be presented elsewhere (E. Stutzmann et al., manuscript in preparation, 2006).

2. Data

[8] We used broadband seismograms from 616 earthquakes (origin time between 1990 and 2002) recorded at one or more of a total of 841 stations from the GEOSCOPE and IRIS global networks and temporary seismograph array

deployments (Figure 1). The data set consists of *P*, *PcP*, *S*, and *ScS* differential traveltimes.

[9] Differential traveltimes were measured using waveform cross correlation on unfiltered, broadband seismograms (Figure 2). For each event we measured direct phase differential traveltimes, P_1-P_2 (or S_1-S_2), for pairs of two stations that recorded the same event. We selected a reference station on which we windowed out manually the direct *P* phase (or *S*). This waveform was then cross correlated with the direct phase recorded at the other stations. The dominant period of the broadband data is about ~1 s for the *P* and ~4 s for the *S* waves, but by correlating the first swing of the phase we effectively measure the high-frequency part of each waveform. We use the Harvard centroid moment tensors (CMTs) to check and, if need be, correct the polarity of a given seismogram. The shifted traces and the corresponding cross correlations were visually inspected for cycle skips, and noisy traces were discarded. We also measured *PcP-P* and *ScS-S* differential traveltimes. For each event-station pair, we windowed out manually the direct phase *P* (and *S*) and this waveform was then cross correlated with a time window comprising *PcP* (and *ScS*) on the same seismogram.

[10] In order to avoid the ambiguity of determining phase arrivals in the triplication range we have considered only data associated with rays that turn beneath the upper mantle discontinuities. The differential traveltimes P_1-P_2 and *PcP-P* were measured on vertical component seismograms, those of S_1-S_2 and *ScS-S* on transverse components. The measured times were corrected for Earth's ellipticity [*Kennett and Gudmundsson*, 1996], and subtraction of time predictions from the one-dimensional (1-D) reference Earth model ak135 [*Kennett et al.*, 1995] then yield the differential traveltime residuals used in the tomographic inversions. We did not determine the reading error for individual measurements, but we estimated the standard error of the *P* wave picks to be ~0.5 s and ~1.0 s for *S*.

[11] Our final data set consists of ~37,000 P_1-P_2 and S_1-S_2 differential traveltime residuals and ~2000 *PcP-P* and *ScS-S* differential traveltime residuals. Figure 3 shows *P* and *S* residuals as a function of ray turning depth of the deepest phase used in the calculation of the time differentials. Most *P* residuals are between −4 and +4 s, whereas most *S* residual are between −8 and +8 s. For the region under study there is no significant correlation between data variance and the depth of the turning point in the lower mantle.

3. Methodology

3.1. Inversion

[12] We parameterized the mantle volume under study by means of nonoverlapping cells with horizontal dimensions of $2° \times 2°$ in 22 layers of approximately the same thickness. The horizontal dimension corresponds to about 220 km at the surface of the Earth and about 100 km at the base of the mantle. The system of linear equations relating slowness perturbations to differential traveltime residuals is given by equation (1). This formulation was used to obtain both the *P* and *S* wave tomographic models by joint inversion of *P* and *S* wave data. We recall that our data are measured at relatively high frequencies, which justifies the use of geometrical raypaths instead of more elaborate finite fre-

quency kernels to calculate the sensitivity matrices. We determined the sensitivity matrix **G** by tracing rays through the reference model.

$$
\begin{matrix} \mathbf{G} & \mathbf{m} & = & \mathbf{d} \end{matrix}
$$
$$
\begin{bmatrix} \mathbf{P\ matrix} & \mathbf{0} \\ \mathbf{0} & \mathbf{S\ matrix} \end{bmatrix} \begin{bmatrix} \delta\mathbf{u_P} \\ \delta\mathbf{u_S} \end{bmatrix} \begin{bmatrix} \delta\mathbf{t_P} \\ \delta\mathbf{t_S} \end{bmatrix}, \quad (1)
$$

where the model vector **m** represents slowness perturbations relative to ak135, the data vector **d** contains measured differential traveltime residuals, and the partial derivative matrix **G** contains the length of the ray segments in each cells. Since the system of equations is underdetermined we select a solution by means of regularization (damping); we use a combination of norm damping, λ, which minimizes slowness perturbations with respect to the reference model, and smoothing (also known as gradient damping), μ, which penalizes against roughness and effectively minimizes slowness differences between adjacent cells. The tomographic system becomes

$$
\begin{pmatrix} \mathbf{G} \\ \lambda\mathbf{I} \\ \mu\mathbf{L} \end{pmatrix} \mathbf{m} = \begin{pmatrix} \mathbf{d} \\ \mathbf{0} \\ \mathbf{0} \end{pmatrix}, \quad (2)
$$

where **I** is the identity matrix and **L** is the gradient operator. We used the LSQR iterative conjugate gradient algorithm [*Paige and Saunders*, 1982a, 1982b; *Nolet*, 1985], to minimize the function:

$$
\|\mathbf{G} \cdot \mathbf{m} - \mathbf{d}\|^2 + \lambda^2\|\mathbf{m}\|^2 + \mu^2\|\mathbf{L} \cdot \mathbf{m}\|^2 = \min .
$$

[13] The regularization parameters λ and μ are determined empirically from a large series of tests with real and synthetic data. We used both the variance reduction and χ^2 to choose the optimal λ and μ from the range 50 to 500. We kept all tomographic models that produced a variance reduction of at least 90% and a value of $\chi2$ between 1.0 and 1.2. All models were obtained after 200 iterations but the system converges quickly and most of the variance reduction is achieved within the first 10–20 iterations. The model discussed in the next sections is obtained with λ = 200 and μ = 400.

3.2. Resolution Tests

[14] We used checkerboard tests to evaluate the ability of a given data coverage and inversion technique to recover mantle structure. For the path coverage associated with the measured data we calculated synthetic traveltimes from several input slowness models. The inversion was performed with the same smoothing and damping parameters as in the inversion of measured data. No errors were assigned to the synthetic data. The resolution is considered adequate when the checkerboard input image can be reconstructed from the synthetic data. Figure 4 illustrates results of tests with an input pattern of different wavelengths: $6° \times 6°$ and $10° \times 10°$. We note that 6° (10°) corresponds to ~550 km (920 km) in the layers near the top of the lower mantle and ~300 km (600 km) near the core mantle boundary.
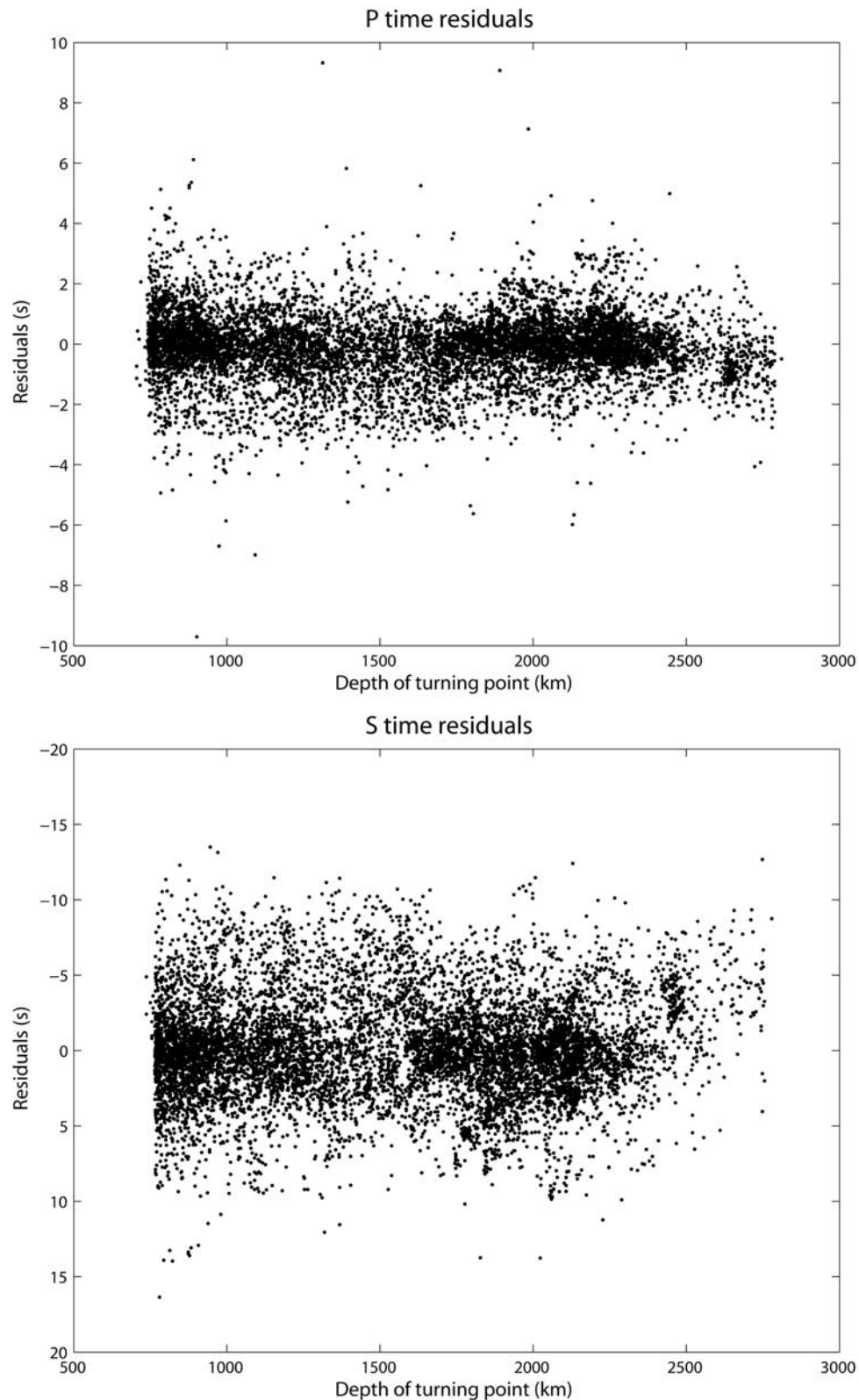
Figure 3. Differential traveltimes (top) P_1-P_2 and (bottom) S_1-S_2 residuals as a function of the turning point depth.

[15] We only display values in cells that are sampled well by P and S wave paths in order not to compromise the comparison of the models. Both models are well recovered down to about 1600 km depth. Below 1700 km depth, the resolution decreases beneath northeast America owing to reduced ray coverage for both P and S waves. At the base of the mantle, only the area beneath Central America is well resolved. We estimated that the minimum size of the
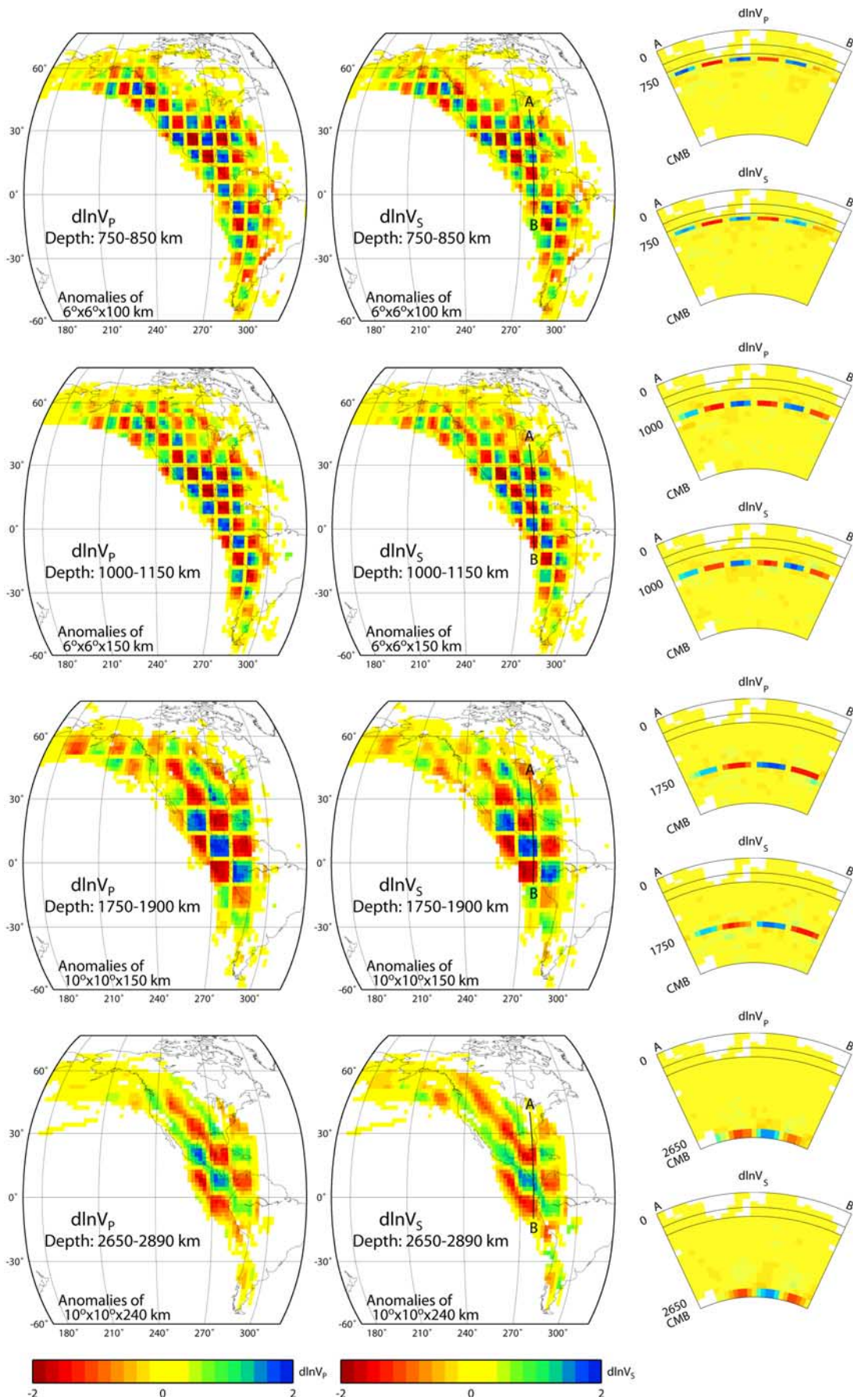
Figure 4

anomaly that can be recovered is ~500 km in the area with good data coverage. More important, Figure 4 shows that as expected from the, by design, similar data coverage, P and S heterogeneity is similarly resolved and that therefore comparison of the two models is meaningful both for the anomaly pattern and amplitude. We note, however, that the vertical path difference between P and S wave can be as large as 200 km for the largest epicentral distances considered here. This could be accounted for with 3-D finite frequency kernels, but that is not done here. We have also performed tests considering a synthetic slab of 1000 km wide and 200 km width located either in the upper mantle or in the lower mantle and we have checked that our $d$lnV_P and $d$lnV_S lower mantle models are not contaminated by upper mantle structures.

4. Tomographic Models

[16] The acceptable models (that is, variance reduction over 90% and χ2 between 1.0 and 1.2) are visually similar, but we considered the small differences that do occur when determining the robust features in the images. Because it is impractical to represent the lateral variation of all models, we show the lateral variations according to one of them. Because (1) resolution of the upper mantle structure is highly variable owing to the uneven earthquake and station distribution and (2) we used only data with lower mantle turning rays, we interpret our models only in the lower mantle part of our model. Our V_P and V_S models are in agreement with coinciding parts of published global models [*Kárason and van der Hilst*, 2001; *Grand*, 1994, 2002] but show more resolved detail.

[17] Figure 5 shows the lateral variations in compressional and shear speeds for six depths in the lower mantle. Beneath the Aleutians we infer fast velocities down to ~1200 km depth and again near the bottom of the mantle. At 800 km depth, V_P and V_S wave speeds are low beneath the transition from the Pacific Ocean and the American continents, and fast anomalies are observed farther east. At larger depths the amplitude of the slow anomaly decreases, and between 900 and 1800 km depth the fast anomaly seems to be connected along a roughly south-north direction from Peru to Alaska. Near 2200 km depth we discern on the V_S map three separate fast anomalies beneath North, Central, and South America; these anomalies are less pronounced on the P wave maps. Finally, in the lowermost mantle the fast S wave anomaly is very broad beneath Central America, which is the best resolved area at that depth, whereas the fast anomaly is smaller both in size and in amplitude in the P wave model.

5. Discussion

[18] When constructing the 4-D framework implied in the correlating of tomographically inferred heterogeneity in the lower mantle with certain episodes of plate tectonic history we face several challenges. First, the interpretation of the tomographic images is neither straightforward nor unique. As shown above, the spatial resolution is highly variable, and nowhere perfect, and relating wave speed perturbations to changes in temperature associated with up or downwellings in the mantle can be a dangerous oversimplification. Second, the tectonic history is complicated and not completely known. Owing to plate fragmentation, the number and size of the oceanic plates that arrived at the trench and, closely related, the directions and rates of plate motion have been changing rather dramatically over time. Combined with substantial motion (in, for instance, the hot spot reference frame) of the overriding continental plates, this has resulted in a complex spatial and temporal pattern of the rates and directions of relative plate motion along the west coast of the Americas, with episodes of convergence, divergence, and strike slip occurring at different places and at different times. This has serious ramifications for the construction and interpretation of cross sections through the tomographic models. Second, without rigorous dynamical modeling associating plate motion and plate features at the surface to flow rates and structure at depth is necessarily *ad hoc*. With these difficulties in mind we discuss the tectonic reconstructions before interpreting the tomographically inferred mantle heterogeneity.

5.1. Plate Tectonic History Reconstructions

[19] We computed the past positions of North and South American active margins for the last 120 Myr (Figure 6) using the Indo-Atlantic hot spot reference frame of *Müller et al.* [1993]. We then attempted to estimate for some key points the Pacific seafloor convergence with respect to the ancient active margins of North, Central, and South America. We used the same method as *Engebretson et al.* [1985], which assumes little or no motion between Pacific and Indo-Atlantic hot spot reference frames. The relative motion of Pacific, Kula, Nazca, Cocos, and Farallon plates is combined with the Pacific hot spot track to obtain the motion of these plates with respect to the Pacific hot spots. The motion of the Americas is computed with respect to the Indo-Atlantic hot spot reference frame and the convergence between the Americas and the plates of Pacific, Kula, Nazca, Cocos, and Farallon is computed as a function of age (arrows in Figure 6). Tomographic cross sections along these paths (Figure 6) are discussed in section 5.2. Convergence velocities with respect to time are computed along three of these cross sections: path B-B′, which can be associated with Farallon and Kula convergence with respect to North America (Figure 7a); path D-D′, which concerns the Cocos and Farallon plate motion relative to Central America (Figure 7b); and path E-E′, which corresponds to the Nazca and Farallon plates with respect to South America (Figure 7c). The corresponding length of subducted slabs is also plotted on Figure 7c.

[20] This estimation is probably imperfect since updated kinematics and robust paleomagnetic analysis [e.g., *Norton*, 1995; *Tarduno and Cottrell*, 1997] have provided evidence for inter hot spot motion within the Pacific or even between

Figure 4. Examples of checkerboard resolution tests with different sizes of input anomalies: Anomalies size 6° × 6° in the layers 750−850 km and 1000−1150 km, anomalies size 10° × 10° in the layers 1750−1900 km and 2650−2890 km. (left) P wave and (middle) S wave anomalies after inversion. (right) Cross section through the P wave and S wave inverted models.
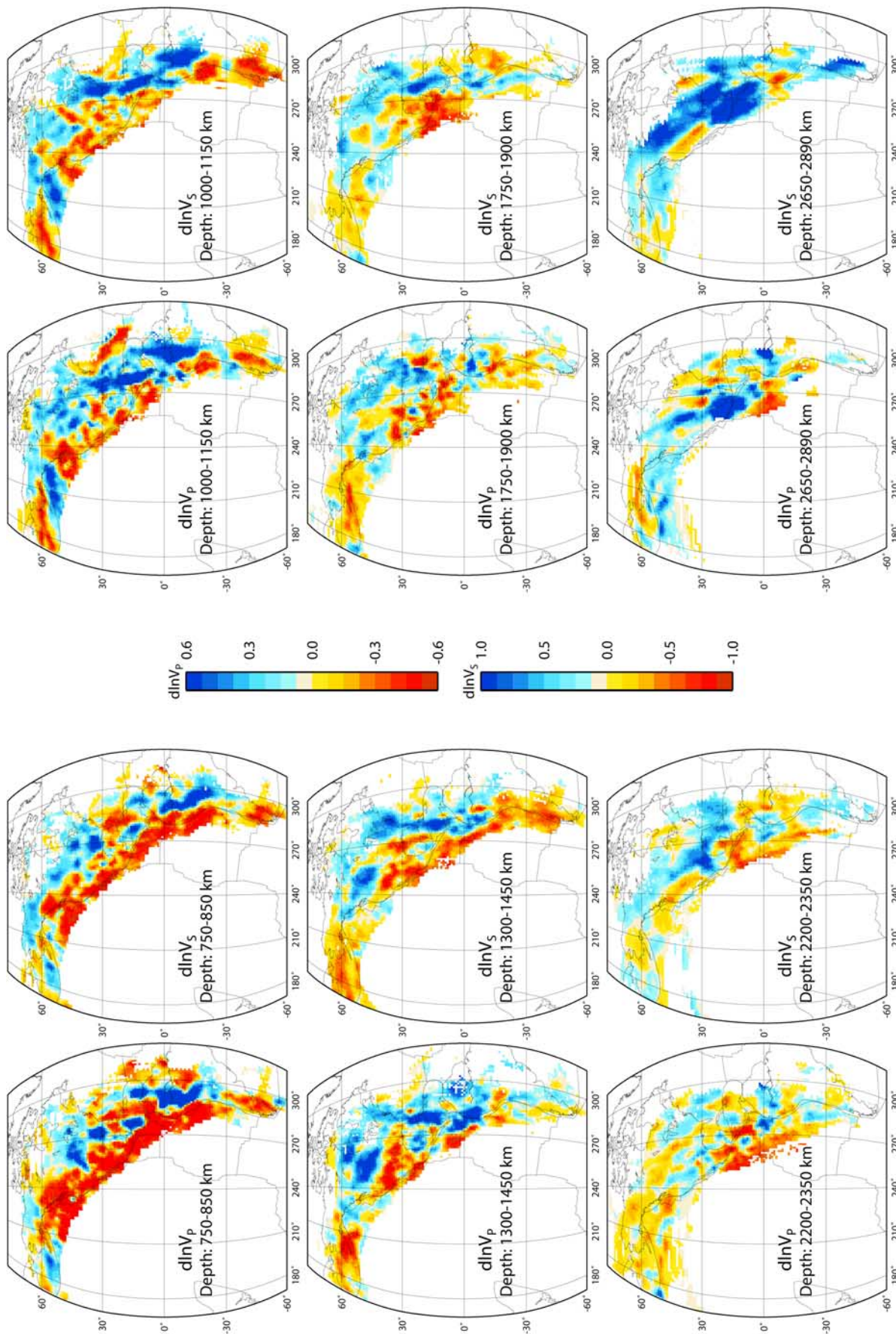
Figure 5. *P* wave and *S* wave velocity perturbation maps with respect to the ak135 reference model in the layers: 750–850 km, 1000–1150 km, 1300–1450 km, 1750–1900 km, 2200–2350 km, and 2650–2890 km. Cells that are not resolved are left white.
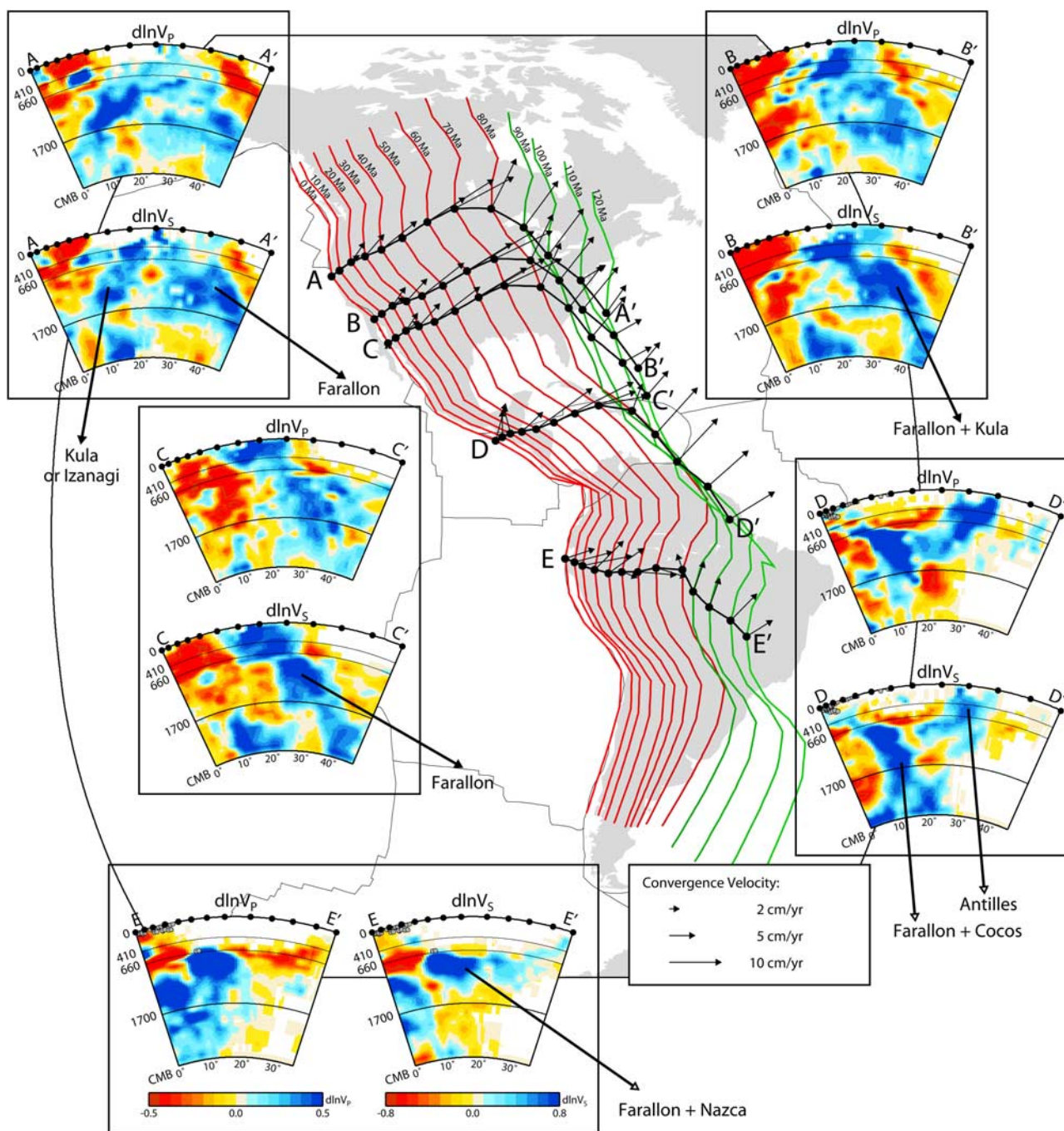
Figure 6. Cross sections through the model for *P* and *S* wave velocities. Red and green lines represent past boundary positions between Pacific seafloor and American continents since 120 Myr (computed from present boundary positions with rotation poles data in the hot spots reference frame). Black lines represent different cross sections made in our V_P and V_S models; different points along the lines represent past margin positions between 120 Myr and 0 Myr ago for given points in the present-day. Arrows represent velocities and directions of convergence at different ages, computed in the hot spots reference frame.

the Pacific and Indo-Atlantic oceans. *Courtillot et al.* [2003] discussed this problem and concluded that the primary hot spots form two mobile subsets, one in each of the two geodynamically distinct hemispheres. *Steinberger and O'Connell* [1998, 2000] and *Steinberger* [2000] showed that the observed geometry and age distribution of hot spot tracks could be explained by upwellings that originate in the

lower mantle but are advected by mantle below. For comparison, we used an independent method, which estimates convergence velocities using a plate circuit passing through Antarctica (also plotted on Figures 7a, 7b, and 7c). We used the detailed kinematic analysis of *Müller et al.* [1993] to compute relative rotations between North America, South America, and East Antarctica. They were com-

bined with kinematic data of *Cande and Kent* [1995], *Cande et al.* [2000], *Norton* [1995], and *Mayes et al.* [1990] in order to obtain the East Antarctica/Pacific motion in different cases. We used the parameters of *Engebretson et al.* [1985] for Kula and Farallon relative to Pacific. Finally, the relative motion of Nazca and Cocos with respect to

Pacific is based on the parameters of *Mayes et al.* [1990] and *Royer et al.* [1992]. As for the hot spots reference frame method, such estimation is imperfect. Indeed, it raises the well-known problem of establishing a reliable kinematic connection between the Indian and Pacific oceans, with the question of the relative motions of East versus West
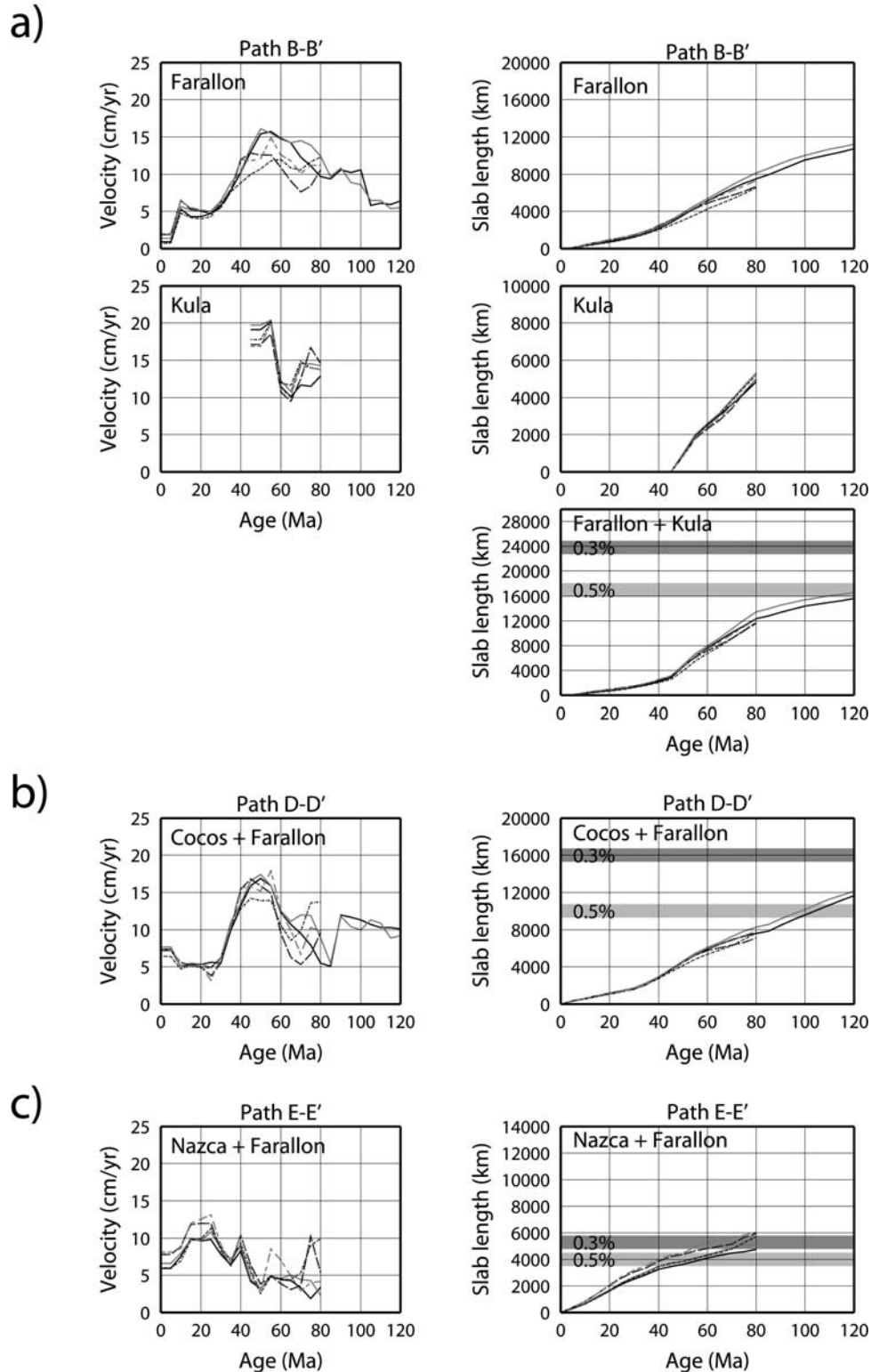

Figure 7

Antarctica. This question has been addressed recently by *Raymond et al.* [2000] and *Cande et al.* [2000], who discussed the importance of a newly discovered extinct plate boundary within the Adare trough in addition to the well-known Mesozoic extension between East and West Antarctica. Fortunately, the two methods yield similar convergence velocities and plate length estimates for the past 80 Myr. Prior to 80 Myr, however, convergence velocities calculated from plate circuit reconstructions are systematically higher than those corresponding to the fixed hot spot reference frame, and at 120 Myr they differ by as much as 10 cm/yr.

5.2. Slab Structures and Plate Boundary Positions

[21] In this section we consider the *S* wave velocity maps because slabs of subducted lithosphere are expected to have a stronger V_S than V_P signature [*Kennett et al.*, 1998; *Ricard et al.*, 2005]. To help identify fragments of subducted lithospheric plates within the mantle, we make the following initial assumptions (which will be verified later): (1) beneath the Americas, the slab fragments sink more or less vertically in the mantle and they enter in the lower mantle without significant deflection around the 670 km depth. This is in agreement with all tomographic model of that area [e.g., *Grand*, 1994; *van der Hilst et al.*, 1997; *Bunge and Grand*, 2000, *Fukao et al.*, 2001]; (2) the plates sink in the upper mantle at the speed of plate convergence, and (3) they are slowed by a factor of four upon entering the high-viscosity lower mantle.

[22] With an average speed of convergence between the oceanic plates and the American continent of ∼8 cm/yr over the past 120 Myr (Figure 7), the vertical flow rates are ∼8 cm/yr and ∼2 cm/yr in the upper and lower mantle, respectively. At these rates, a vertically sinking plate would reach the base of the mantle in 120 Myr. In this simplified framework, remnants of oceanic lithosphere that subducted prior to 120 Myr ago are expected at or near the core mantle boundary, whereas the seismically fast anomalies in the shallower mantle result from, and can perhaps be correlated with, more recent episodes of subduction.

[23] Figure 8 shows V_S tomographic maps along with a plate history reconstruction from *Lithgow-Bertelloni and Richards* [1998], nearly identical to that of *Engebretson et al.* [1985] for the motion of the Pacific plates. The tomographic model is plotted together with the coast lines of the Americas at present time. To allow the evaluation of subduction related mantle heterogeneity in the framework of past plate motion (Figure 8, right), we must consider the relative motion of the overriding continental plates. There-

fore Figure 8 depicts the positions of plate boundaries for the past 120 Myr as well as the velocity vectors at five distinct ages.

[24] Figure 6 shows that the Americas moved toward the northwest prior to ∼70–80 Myr and that more recently North America moved toward the west, and South America toward the northwest. The latter difference results in a small relative convergence between North and South America (probably accommodated in the Caribbean region). The change from northwest to (south) westward has to be taken into account when constructing the mantle cross sections shown in Figure 6. For instance, cross sections B-B′ and C-C′ are in the same overall area as those presented by *Grand et al.* [1997], but our depiction of the deep part of the fast anomaly depth is slightly different because our cross sections are chosen to be in the direction of relative motion of the overriding plate, whereas Grand et al.'s cross sections are mostly perpendicular to the present-day plate boundary.

[25] In the upper part of the lower mantle (Figure 8a; 750–850 km depth) we can recognize the imprint of the most recent phase of the plate history considered here. The distinctive fast anomalies are associated with subduction of the Nazca and Cocos plates beneath South and Central America, respectively, the Juan de Fuca plate beneath North America, and the Pacific plate beneath the Aleutian island arc. The fast anomaly beneath the eastern part of the Caribbean region can be explained by subduction of the Atlantic ocean floor along the Lesser Antilles arc [e.g., *van der Hilst*, 1990]. To see how the successive breakup of the proto-Farallon plate into these fragments is reflected in mantle heterogeneity beneath the Americas, we discuss mantle structures from the base of the mantle upward along with the history of plate motion from ∼120 Myr to some 10 Myr ago.

[26] In the lowermost mantle (Figure 8e; 2650–2890 km) most of the *S* wave velocity map is fast, with notable exceptions between 0° and −15°S and between 30° and 45°N, beneath what is now the west coast of the Americas; here the images reveal two distinct low-velocity anomalies. Resolution at this depth is relatively poor beneath the southern part of South America, but the data do reveal a fast anomaly. This structure could represent part of the Phoenix plate. Subduction of the Phoenix plate, the oldest (known) offspring of the proto-Farallon plate, stopped 80–90 Myr ago, and most of it may now be at near the base of the mantle beneath South America. Farther north, the large fast anomaly between the equator and Alaska may represent ancient parts of the Farallon plate, which was moving north to northwestward between 120 and 85 Myr, and subducting

Figure 7. (a) (left) Convergence velocities between 0 Myr and 120 Myr for the Farallon and Kula plates along the North American continent. Solid black and gray lines denote calculations in the hot spots reference frame using the absolute motion of *Engebretson et al.* [1985] for Pacific and American plates and the absolute motion of *Engebretson et al.* [1985] for the Pacific plate and that of *Müller et al.* [1993] for the American plate, respectively. Black and gray dashed lines denote reconstructions from plate circuit through Farallon/Kula, Pacific, Antarctica, Africa, and North America. The relative motion of Farallon/Kula to Pacific is from *Engebretson et al.* [1985]; that of Pacific to Antarctica is from *Cande and Kent* [1995] and it *Cande et al.* [2000] (black dotted line), *Norton* [1995] (black dashed line) and *Mayes et al.* [1990] (light gray dashed line); that of Antarctica to the North America is from *Müller et al.* [1993]. (right) Slab lengths as a function of time calculated from convergence velocities on the left; for the Farallon, Kula and the two together, respectively. (b) Same as Figure 7a, but for the Cocos and Farallon plates along the Central American continent. The relative motion of Cocos to Pacific is from *Royer et al.* [1992]. (c) Same as Figure 7a, but for the Nazca and Farallon plate along the South American continent. The relative motion of Nazca to Pacific is from *Royer et al.* [1992].
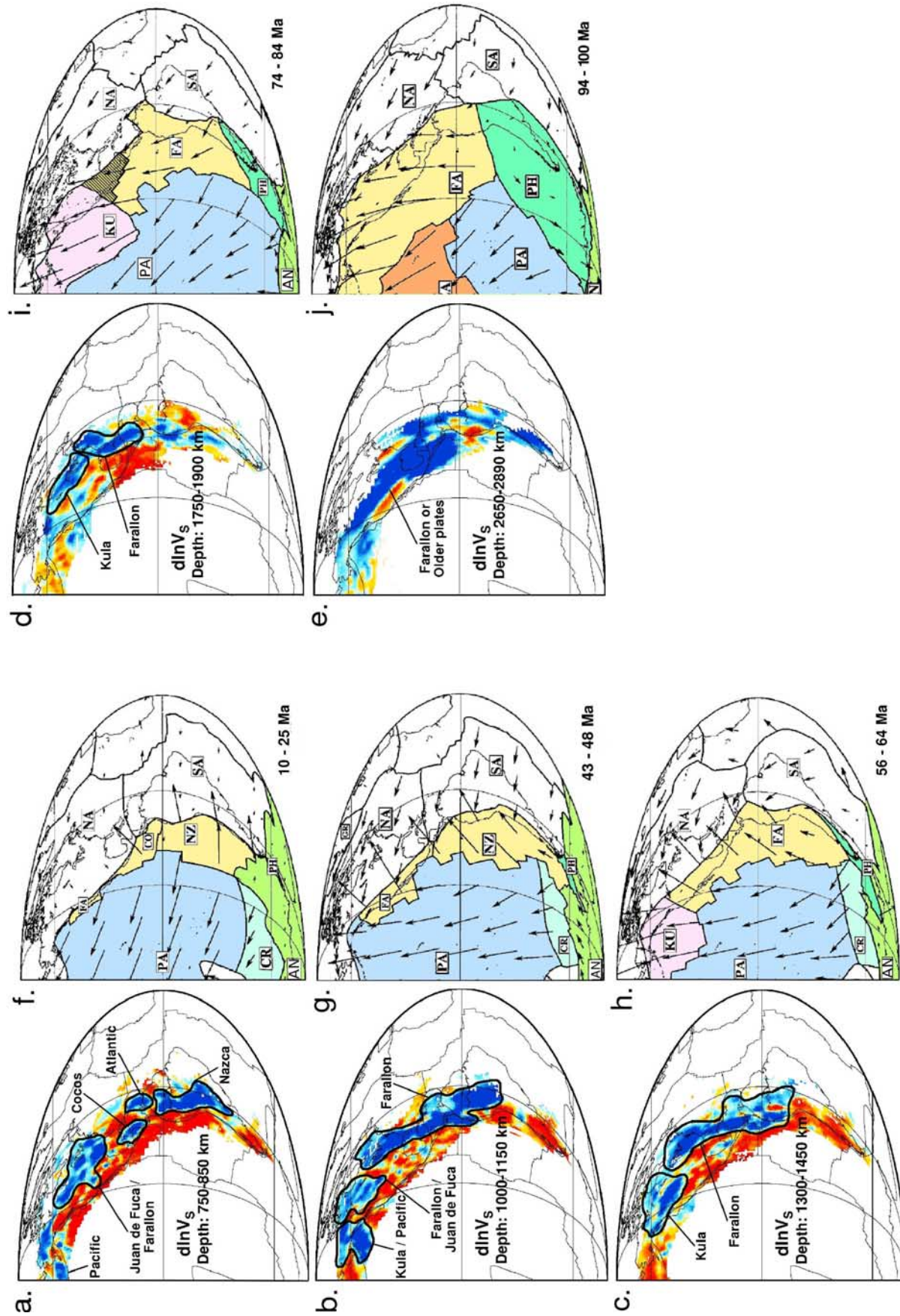
REN ET AL.: LOWER MANTLE BENEATH THE AMERICAS

Figure 8. (a, b, c, d, e) *S* wave velocity perturbation maps with respect to the ak135 reference model in the layers: 750–850 km, 1000–1150 km, 1300–1450 km, 1750–1900 km and 2650–2890 km. (f, g, h, i, j) Maps of plate location and convergence location at different ages are from *Lithgow-Bertelloni and Richards* [1998].

beneath North America and the Aleutians. Remnants of plates that subducted in the area prior to 120 Myr may, of course, also contribute to the structure at the base of the mantle.

[27] About 80 Myr ago, the Farallon plate broke up into two plates (Figure 8i). The northern part, the Kula plate, continued to move northward whereas the southern part, the Farallon plate proper, changed motion clockwise to a northeasterly direction with respect to North America at ~65 Myr. The location of the ancient Kula-Farallon ridge has been disputed. According to *Engebretson et al.* [1985], at ~80 Ma the ridge and the adjacent thin lithosphere was located along the northwestern part of Central America (shaded area in Figure 8i). At 1750–1900 km depth this region is marked by distinctly low *S* wave speed (Figure 8d); any association with subduction of the ridge is tenuous, at best, but the position at different depths in the mantle of the slow "corner" adjacent to the bend in the slab is a useful marker for discussing the motion of the Kula-Farallon contact relative to North America (see below).

[28] Figure 8d also shows that to the northeast of this area the fast slab-like *S* wave anomaly is divided into NW-SE trending structure beneath Canada and a N-S trending structure beneath Central and South America. In this discussion we associate the northern structure with the Kula plate and the southern part with the Farallon plate. At 1750–1900 km depth the "bend" between the Kula and Farallon plates is located just to the south of the Great Lakes; using the past locations of the west coast (Figure 8i), we infer that this is where the northern part of the Gulf of California was located some 80 Myr ago. This relationship supports our interpretation that the Kula-Farallon plate boundary, which was at the trench 80 Myr ago, is now located between 1750 and 2200 km depth. *Bunge and Grand* [2000] used a similar observation to infer that close to the ancient Kula-Farallon ridge the Farallon plate subducted under a shallow angle whereas Kula subduction was steep. Our results are consistent with this inference, but on the basis of our images we cannot rule out other styles of subduction.

[29] Regardless of the precise location and nature of the Kula-Farallon plate contact, the images shown here support the notion that the Kula-Farallon ridge subducted beneath North America [*Bunge and Grand*, 2000]. Furthermore, the northwestward motion of the Kula-Farallon border with respect to North America between 65 and 56 Myr can be tracked in our images of deep mantle structure. In particular, it is striking to observe that near 1400 km depth (Figure 8c) the above mentioned slow "corner" near the transition of the N-S trending Farallon plate and the NW-SE trending Kula plate is located well north of its location at larger depths (e.g., Figure 8d).

[30] Around 48 Myr, ocean floor spreading between the Pacific-Kula plates stopped (Figure 8g), and the Kula plate thus began moving along with the Pacific plate [*Engebretson et al.*, 1985; *Lithgow-Bertelloni and Richards*, 1998]. At that time, much of the Farallon plate had subducted beneath the Americas, and the Pacific plate converged to and made contact with North America near the west coast of Canada and close to the Gulf of California. The part of the Farallon plate left in between these regions is now called the Juan de Fuca plate, which is subducting beneath North

America at the Cascadia subduction zone (Figure 8f). The northernmost plate boundary was the former Kula-Farallon ridge; in the south the boundary was formed by the ridge between Pacific and Farallon plates (that is, the predecessor of the present-day East Pacific Rise (EPR)). On our tomographic maps between 900 and 1200 km depth (Figure 8b) we observe several fast anomalies separated by slow regions. We interpret these anomalies as the Pacific/Kula slab at the north, the Farallon/Juan de Fuca slab beneath Canada, and the Farallon slab beneath eastern North America and beneath Central America. We speculate that two distinct seismically slow structures on both sides of the Farallon/Juan de Fuca slab mark the location of the two ancient spreading ridges.

[31] At even shallower depth we recognize, as mentioned above, the fast anomalies associated with subduction of (from south to north along the west coasts of the Americas) the Nazca, Cocos, Juan de Fuca, and Pacific plates. The fast anomaly beneath the Aleutians is farther west with respect to its location in the layer 1000–1150 km depth, which is consistent with the abrupt northwestward change in Pacific plate motion ~43 Myr ago [e.g., *Engebretson et al.*, 1985]. We also note that the slow anomalies around the Cocos plate most likely represent the ridges (EPR in the north and Galapagos ridge in the south) that began fragmenting the Farallon into the Cocos and Nazca plates ~25 Myr ago [e.g., *van der Hilst*, 1990]. At this depth one can also discern the wave speed anomaly associated with the subduction of Atlantic lithosphere beneath the Lesser Antilles arc (290W, 15N) [see, e.g., *van der Hilst and Spakman*, 1989].

[32] In conclusion, we observe a very good correlation between the plate history reconstruction and our *S* wave tomographic images at different depth. Our model may not show the entire Farallon plate, which may extend farther north and east, but we can track the fragmentation of Farallon plate with time. Keeping these comparisons and their limitations in mind we can now interpret cross sections on Figure 6. On the northern cross section (path A-A′ on Figure 6), the large anomaly dipping toward the west may be Juan de Fuca in the upper part and Kula in its deeper part. Farther east, we may see the Farallon plate down to about 1700 km. At larger depth we have no resolution in that area. An alternative interpretation would be that we see the remnant of the Farallon and Kula plates at the east and Izanagi at the west. The existence of this plate has been proposed by *Engebretson et al.* [1985]. The two cross sections farther south (paths B-B′ and C-C′ on Figure 6) show the Kula and Farallon plate down to the core-mantle boundary, with structural complexity in the upper mantle transition zone. In the section across Central America (path D-D′ on Figure 6) we infer the Farallon plate on the left and the Atlantic plate on the right. Finally, beneath South America (path E-E′ on Figure 6) we infer the Nazca/Farallon plate down to about 1500 km depth but not deeper.

5.3. Volume and Length of Slabs

[33] In order to support the interpretation of our tomographic model in terms of plate history, we have compared the total amount of subducted material estimated from our V_S model and those estimated by plate motion history (Figure 7). Tomography yields a blurred image; the fast

anomalies are likely to be larger than the slab itself, and it is not obvious which anomaly contour marks the slab. To illustrate the sensitivity to this choice, we consider two anomaly cutoffs: 0.3% and 0.5%. For these two values, the slab volumes estimated for paths B-B', D-D', and E-E' are plotted in Figure 7.

[34] Considering an average plate thickness of 100 km, the fast velocity anomaly surface along B-B' correspond to a slab length of 17,000 km (24,000 km) when associated with velocity perturbations higher than 0.5% (0.3%). A 17,000 km long slab can be explained by plate history of the last 100–120 Myr (Figure 7a). If the slab were longer, part of the observed fast anomaly must correspond to older processes, which would not be surprising because subduction in that area has been going on for much longer than 120 Myr.

[35] Along D-D', the slab contour associated with velocity anomalies higher than 0.5% (0.3%) corresponds to a slab length of 9800 km (16,000 km). These slab lengths suggest that the tomographic image corresponds indeed to the subduction history over the last 90 to 120 Myr of Farallon and, subsequently, Cocos plates (Figure 7b). Finally, along E-E' the tomographic image yields a slab length of about 4000 to 5000 km which is consistent with subduction of the Nazca-Farallon plate over the last 50 Myr. For that plate a similar result was reported by *Grand* [1994].

[36] Thus the slab lengths estimated from the slab volume as inferred from our tomographic maps are in agreement with the lengths obtained from plate kinematic reconstruction over the last 90–120 Myr in North and Central America and over the last 50 Myr in South America. This supports our interpretation. We note that this above calculation accounts for the fact that the slab may fold upon penetration into the lower mantle [e.g., *Gaherty and Hager*, 1994; *Ribe et al.*, 2006].

6.   Conclusion

[37] We have used waveform cross correlation to measure 37,000 differential traveltimes ($P_1 - P_2$ and $S_1 - S_2$) and 2000 PcP-P and ScS-S times from earthquakes and receivers along a wide corridor from Alaska to South America. These data were inverted simultaneously to obtain both P and S wave velocity models at regional scale. Comparison of our models with other global models shows good agreement although more resolved details in the lower mantle are observed in our models. In order to unravel subduction history we have computed the convergence of oceanic plates in the Pacific realm with respect to the north and South America. We show that for ages younger than 80 Myr, there is little difference between the plate motion reconstruction derived from the hot spots reference frame and from a plate circuit through Antarctica. Using the fixed hot spots reference frame we have shown that there is a good correlation between our tomographic models at different depths and expectations from the plate history reconstructions over the past 100 Myr. Our interpretation is supported by the agreement of the volume and length of slabs estimated either from the tomographic images or from plate history reconstruction. The ability to reconstruct the fragmentation of Farallon plate from 3-D mantle models

confirms that high resolution seismic tomography can be an important tool for paleogeographers.

References

Albarède, F., and R. D. van der Hilst (2002), Zoned mantle convection, *Philos. Trans. R. Soc. London*, *360*, 2569–2592.

Bijwaard, H., W. Spakman, and E. R. Engdahl (1998), Closing the gap between regional and global travel time tomography, *J. Geophys. Res.*, *103*, 30,055–30,078.

Bird, P. (1979), Continental delamination and the Colorado plateau, *J. Geophys. Res.*, *84*, 7561–7571.

Bird, P. (1984), Laramide crustal thickening event in the Rocky-Mountain foreland and great plains, *Tectonics*, *3*, 741–758.

Bunge, H. P., and S. P. Grand (2000), Mesozoic plate-motion history below the northeast Pacific Ocean from seismic images of the subducted Farallon slab, *Nature*, *405*, 337–340.

Cande, S. C., and D. V. Kent (1995), Revised calibration of the geomagnetic polarity timescale for the late Cretaceous and Cenozoic, *J. Geophys. Res.*, *100*, 6093–6095.

Cande, S. C., J. M. Stock, R. D. Müller, and T. Ishihara (2000), Cenozoic motion between East and West Antarctica, *Nature*, *404*, 145–150.

Christensen, U., and D. A. Yuen (1984), The interaction of a subducting lithospheric slab with a chemical or phase boundary, *J. Geophys. Res.*, *89*, 4389–4402.

Courtillot, V., A. Davaille, J. Besse, and J. Stock (2003), Three distinct types of hotspots in the Earth's mantle, *Earth Planet. Sci. Lett.*, *205*, 295–308.

Davies, G. F. (1995), Penetration of plates and plumes through the mantle transition zone, *Earth Planet. Sci. Lett.*, *133*, 507–516.

Dziewonski, A. M., and J. H. Woodhouse (1987), Global images of the Earth's interior, *Science*, *236*, 37–48.

Engebretson, D. C., A. Cox, and R. G. Gordon (1985), Relative motions between oceanic and continental plates in the Pacific basin, *Spec. Pap. Geol. Soc. Am.*, *206*, 1–59.

Fukao, Y., S. Widiyantoro, and M. Obayashi (2001), Stagnant slabs in the upper and lower mantle transition region, *Rev. Geophys.*, *39*, 291–323.

Gaherty, J. B., and B. H. Hager (1994), Compositional vs. thermal buoyancy and the evolution of subducted lithosphere, *Geophys. Res. Lett.*, *21*, 141–144.

Grand, S. P. (1994), Mantle shear structure beneath the Americas and surrounding oceans, *J. Geophys. Res.*, *99*, 11,591–11,621.

Grand, S. P. (2002), Mantle shear-wave tomography and the fate of subducted slabs, *Philos. Trans. R. Soc. London*, *360*, 2475–2491.

Grand, S. P., R. D. van der Hilst, and S. Widiyantoro (1997), Global seismic tomography: A snapshot of convection in the Earth, *GSA Today*, *7*, 1–7.

Griffiths, R., R. Hackney, and R. D. van der Hilst (1995), A laboratory investigation of effects of trench migration on the descent of subducted slabs, *Earth Planet. Sci. Lett.*, *133*, 1–17.

Gurnis, M., and B. Hager (1988), Controls of the structure of subducted slabs, *Nature*, *335*, 317–321.

Hager, B., R. Clayton, M. Richards, P. Comer, and A. Dziewonski (1985), Lower mantle heterogeneity, dynamic topography and the geoid, *Nature*, *313*, 541–545.

Kárason, H., and R. D. van der Hilst (2001), Tomographic imaging of the lowermost mantle with differential times of refracted and diffracted core phases (PKP, P_{diff}), *J. Geophys. Res.*, *106*, 6569–6587.

Kennett, B. L. N., and O. Gudmundsson (1996), Ellipticity corrections for seismic phases, *Geophys. J. Int.*, *127*, 40–48.

Kennett, B. L. N., E. Engdahl, and R. Buland (1995), Constraints on seismic velocities in the Earth from traveltimes, *Geophys. J. Int.*, *122*, 108–124.

Kennett, B. L. N., S. Widiyantoro, and R. D. van der Hilst (1998), Joint seismic tomography for bulk sound and shear wave speed in the Earth's mantle, *J. Geophys. Res.*, *103*, 12,469–12,493.

Kincaid, C., and P. Olson (1987), An experimental study of subduction and slab migration, *J. Geophys. Res.*, *92*, 13,832–13,840.

Lithgow-Bertelloni, C., and M. A. Richards (1998), The dynamics of Cenozoic and Mesozoic plate motions, *Rev. Geophys.*, *36*, 27–78.

Masters, G., T. H. Jordan, P. G. Silver, and F. Gilbert (1982), Spherical Earth structure from fundamental spheroidal-mode data, *Nature*, *298*, 609–613.

Mayes, C. L., L. A. Lawver, and D. T. Sandwell (1990), Tectonic history and new isochron chart of the South Pacific, *J. Geophys. Res.*, *95*, 8543–8567.

Müller, R. D., J.-Y. Royer, and L. A. Lawver (1993), Revised plate motion relative to the hotspots from combined Atlantic and Indian Ocean hotspot tracks, *Geology*, *21*, 275–278.

Nolet, G. (1985), Solving or resolving inadequate and noisy tomographic system, *J. Comput. Phys.*, *61*, 463–468.

Norton, I. O. (1995), Plate motions in the North Pacific: The 43 Ma none-vent, *Tectonics*, *14*, 1080–1094.

Paige, C. C., and M. A. Saunders (1982), LSQR: An algorithm for sparse linear equations and sparse least squares, *Trans. Math. Software*, *8*, 43–71.

Paige, C. C., and M. A. Saunders (1982), ALGORITHM 583 LSQR: Sparse linear equations and sparse least squares problems, *Trans. Math. Software*, *8*, 195–209.

Raymond, C. A., J. M. Stock, and S. C. Cande (2000), Fast Paleogene motion of the Pacific hotspots from revised global plate circuit constraints, in *The History and Dynamics of Global Plate Motions*, *Geophys. Monogr. Ser.*, vol. 121, edited by M. A. Richards, R. G. Gordon, and R. D. van der Hilst, pp. 359–375, AGU, Washington, D. C.

Ribe, N. M., E. Stutzmann, Y. Ren, and R. D. van der Hilst (2006), Folding instabilities of subducted lithosphere revealed by tomographic imaging, *Earth Planet. Sci. Lett.*, in press.

Ricard, Y., M. Richards, C. Lithgow-Bertelloni, and Y. Le Stunff (1993), A geodynamic model of mantle density heterogeneity, *J. Geophys. Res.*, *98*, 21,895–21,909.

Ricard, Y., E. Mattern, and J. Matas (2005), Synthetic tomographic images of slabs from mineral physics, in *Earth's Deep Mantle: Structure, Composition, and Evolution*, *Geophys. Monogr. Ser.*, vol. 160, edited by R. D. van der Hilst et al., pp. 285–302, AGU, Washington, D. C.

Richards, M. A., and D. Engebretson (1992), Large-scale mantle convection and the history of subduction, *Nature*, *355*, 437–440.

Royer, J.-Y., R. D. Müller, L. M. Gahagan, L. A. Lawver, C. L. Mayes, D. Nürnberg, and J. G. Sclater (1992), A global isochron chart, *Tech. Rep. 117*, Univ. of Tex. Inst. for Geophys., Austin.

Saltzer, R. L., E. Stutzmann, and R. D. van der Hilst (2004), Poisson's ratio in the lower mantle beneath Alaska: Evidence for compositional heterogeneity, *J. Geophys. Res.*, *109*, B06301, doi:10.1029/2003JB002712.

Steinberger, B. (2000), Slabs in the lower mantle—Results of dynamic modeling compared with tomographic images and the geoid, *Phys. Earth Planet. Inter.*, *118*, 241–257.

Steinberger, B., and R. J. O'Connell (1998), Advection of plumes in mantle flow: Implications for hotspot motion, mantle viscosity and plume distribution, *Geophys. J. Int.*, *132*, 412–434.

Steinberger, B., and R. J. O'Connell (2000), Effects of mantle flow on hotspot motion, in *The History and Dynamics of Global Plate Motions*, *Geophys. Monogr. Ser.*, vol. 121, edited by M. A. Richards, R. G. Gordon, and R. D. van der Hilst, pp. 377–398, AGU, Washington, D. C.

Storey, B. C. (1995), The role of mantle plumes in continental break-up: Case histories from gondwanaland, *Nature*, *377*, 301–308.

Tan, E., M. Gurnis, and L. Han (2002), Slabs in the lower mantle and their modulation of plume formation, *Geochem. Geophys. Geosyst.*, *3*(11), 1067, doi:10.1029/2001GC000238.

Tarduno, J. A., and R. D. Cottrell (1997), Paleomagnetic evidence for motion of the Hawaiian hotspot during formation of the Emperor seamounts, *Earth Planet. Sci. Lett.*, *153*, 171–180.

van der Hilst, R. D. (1990), Tomography with *P*, *PP*, and *pP* delay-time data and the three-dimensional mantle structure below the Caribbean region, Ph.D. thesis, Utrecht Univ., Utrecht.

van der Hilst, R. D., and H. Kárason (1999), Compositional heterogeneity in the bottom 1000 kilometers of Earth's mantle: Toward a hybrid convection model, *Science*, *283*, 1885–1888.

van der Hilst, R. D., and T. Seno (1993), Effects of relative plate motion on the deep structure and penetration depth of slabs below the Izu-Bonin and Mariana island arcs, *Earth Planet. Sci. Lett.*, *120*, 395–407.

van der Hilst, R. D., and W. Spakman (1989), Importance of the reference model in linearized tomography and images of subduction below the Caribbean Plate, *Geophys. Res. Lett.*, *16*, 1093–1096.

van der Hilst, R. D., S. Widiyantoro, and E. R. Engdahl (1997), Evidence for deep mantle circulation from global tomography, *Nature*, *386*, 578–584.

Vasco, D. W., and L. R. Johnson (1998), Whole Earth structure estimated from seismic arrival times, *J. Geophys. Res.*, *103*, 2633–2671.

Zhao, D. (2004), Global tomographic images of mantle plumes and subducting slabs: Insight into deep Earth dynamics, *Phys. Earth Planet. Inter.*, *146*, 3–34.

————————————

J. Besse, Laboratoire de Paléomagnétisme, Institut de Physique du Globe de Paris, 4 Place Jussieu, F-75252 Paris cedex 05, France. (besse@ipgp.jussieu.fr)

Y. Ren and E. Stutzmann, Laboratoire de Sismologie UMR 7580, Institut de Physique du Globe de Paris, 4 Place Jussieu, F-75252 Paris cedex 05, France. (ren@ipgp.jussieu.fr; stutz@ipgp.jussieu.fr)

R. D. van der Hilst, Department of Earth, Atmospheric, and Planetary Sciences, Massachusetts Institute of Technology, Cambridge, MA 02139, USA. (hilst@mit.edu)